

# EMF-Efficient MU-MIMO Networks: Harnessing Aerial RIS Technology

Mariam Chemingui , Ahmed Elzanaty , Rahim Tafazolli 

Institute for Communication Systems (ICS), University of Surrey, UK

**Abstract**—The rollout of the fifth-generation (5G) networks has raised some concerns about potential health effects from increased exposure to electromagnetic fields (EMF). To address these concerns, we design a novel EMF-aware architecture for uplink communications. Specifically, we propose an aerial reconfigurable intelligent surface (ARIS) assisted multi-user multiple-input multiple-output (MIMO) system, where the ARIS features a reconfigurable intelligent surface (RIS) panel mounted on an unmanned aerial vehicle (UAV), offering a flexible and adaptive solution for reducing uplink EMF exposure. We formulate and solve a new problem to minimize the EMF exposure by optimizing the system parameters, such as transmit beamforming, resource allocation, transmit power, ARIS phase shifts, and ARIS trajectory. Our numerical results demonstrate the effectiveness of EMF-aware transmission scheme over the benchmark methods, achieving EMF reductions of over 30% and 90% compared to the fixed ARIS and non-ARIS schemes, respectively.

**Index Terms**—5G, electromagnetic field (EMF), EMF-aware design, multi-user MIMO, aerial reconfigurable intelligent surface (ARIS).

## I. INTRODUCTION

Nowadays, the widespread deployment of fifth-generation (5G) technology has raised concerns among certain segments of the population regarding the potential exposure to electromagnetic fields (EMF) emitted by 5G networks [1], [2]. The potential for heightened EMF exposure is contingent not only upon network architecture but also on the characteristics of the utilized devices. Recently, France has halted the sales of the iPhone 12 due to its higher radiation levels exceeding regulatory limits [3].

Studies have indicated that electromagnetic (EM) radiations can have both thermal and non-thermal effects on the human body [4]–[6]. The thermal effects occur when the body absorbs excessive EM radiation, leading to the production of heat that can potentially damage tissues. However, the scientific community continues to engage in ongoing debates regarding the potential long-term non-

thermal effects of EM radiation on human health [7]–[9]. Nevertheless, certain investigations have documented discernible biological manifestations attributed to exposure to non-ionizing EMF [10], [11]. In this context, the International Agency for Research on Cancer (IARC) has categorized radio frequency radiation as “Possibly carcinogenic to humans” (Group 2B) [12].

To address the public concern, regulatory agencies such as the Federal Communications Commission (FCC) [13] and the International Commission on Non-Ionizing Radiation Protection (ICNIRP) [14], have established guidelines to ensure that the EMF exposure is quantified and limited on the users’ side. However, EMF exposure refers to the radiation exposure generated by the propagation of the EM waves, which are usually emitted by wireless terminals such as base stations (BSs) and user equipment (UE). Since UEs are much closer to the human body compared to BS, in general, the uplink EMF exposure from them is dominant, i.e., approximately ten times stronger than the downlink exposure [15]–[17]. The dominance of uplink exposure is further supported by studies in large-scale cellular networks [18], [19].

To evaluate EMF exposure during uplink (UL) transmission, the standard specific absorption rate (SAR) metric, which measures the amount of electromagnetic power absorbed by human tissue per unit mass, is utilized [20], [21]. Consequently, many governments require that uplink EMF exposure, as assessed by SAR, remains below specified thresholds. In response to this, precautionary measures should be taken while designing future cellular systems.

### A. Related Work

In the 5G cellular systems, the prevalence of connected devices with multiple antennas has evoked EMF-aware design for the uplink transmission. For

example, authors in [22] proposed a beamforming-based technique for minimizing the EMF exposure in the uplink transmission design. In [23], the authors provided a model to assess the individual exposure with multi-antenna user terminals operating in a multi-carrier environment by optimizing the relative phase differences and power allocation between the antenna ports. However, when considering higher frequency bands, the line-of-sight (LoS) blockage needs to be accounted for, as it can significantly influence the distribution and intensity of electromagnetic fields and subsequent exposure levels, as the users may need to increase their transmit power to compensate for the high path-loss [24].

Recently, due to the proposal of the controllable intelligent radio environments, the reconfigurable intelligent surface (RIS) has been introduced to mitigate the effect of LoS blockages in terrestrial and non-terrestrial networks [25], [26]. The RIS is a passive reflector that superimposes the incident signal waves by adjusting the phase shifts and then reflects them in the appropriate directions [27], [28]. Consequently, optimizing the phase shifts enhances the channel, enabling a reduction in transmit power without compromising the data rate [29]. In [24], phase shifts of the RIS were designed to reduce the exposure for uplink multi-user single-input multiple-output (SIMO) systems. Note that the fixed placement of the RIS may constrain its ability to effectively mitigate network blockages and optimize exposure reduction in scenarios characterized by dynamic changes in signal propagation. A possible solution for mobility is considering unmanned aerial vehicle (UAV)-assisted networks [30]–[32]. In a notable example, the work in [33] presented an approach involving tethered UAVs equipped with receive-only antennas, aiming to minimize EMF exposure while ensuring high quality of service (QoS) for users. However, using tethered UAVs introduces constraints on mobility, resulting in reduced degrees of freedom when designing the network architecture. Furthermore, the restricted mobility of the tethered UAVs may hinder their ability to adapt to dynamic propagation environments or to effectively satisfy evolving user requirements. Nevertheless, the ongoing investigation into RIS has led to the introduction of a novel architecture known as aerial reconfigurable intelligent surface (ARIS). Distinguishing itself from traditional RIS, the ARIS can

be installed on aerial platforms like UAVs, enabling the establishment of more robust LoS connections [34]. Moreover, the ARIS exhibits the capability to dynamically adjust its position, allowing it to adapt to various propagation environments.

In this context, we propose a two-fold design aimed at minimizing EMF exposure. Firstly, we introduce ARIS to achieve finer control over transmit beamforming, thereby reducing the coupling between antennas and users' bodies and minimizing the induced SAR. Secondly, we adopt a power control scheme that reduces transmit power while ensuring QoS for all network users. By optimizing the propagation environment through the design of ARIS phases and trajectory, we enhance uplink communication with LoS links, thereby reducing the required transmit power. Additionally, resource and power allocation are managed to meet QoS requirements effectively. Our novel architecture, incorporating ARIS, dynamically adjusts propagation environment to minimize population EMF exposure, offering a cost-effective and sustainable solution for reducing radiation in various scenarios characterized by a low probability of LoS links. To the best of our knowledge, EMF-efficient architectures and associated algorithms involving ARIS have not been previously discussed in the literature.

## B. Contributions

In this paper, we propose a novel architecture for EMF-aware multi-user multiple-input-multiple-output (MU-MIMO) cellular systems, where the exposure is further reduced beyond the standards as precautionary measure. More precisely, we consider ARIS to assist uplink communications, aiming to reduce the overall EMF exposure for the population while assuring the required transmit data rates for users. In fact, having a RIS carried on a mobile UAV can provide additional degrees of freedom in network design, bringing several benefits such as providing *(i)* flexible deployment for RIS, especially in dynamic networks; *(ii)* an indirect LoS, with high probability, through the RIS due to the relatively high altitude of the UAV; and *(iii)* EMF-efficient solution by using lower transmit power while maintaining QoS standards, benefiting from improved signal-to-noise ratio (SNR) due to the large number of RIS elements.

The main contributions of this paper are summarized as follows.

- We propose a novel EMF-aware design where the transmit beamforming parameters, the phase-shift matrix of the RIS, the resource element (RE) allocation vector, the transmit power of the multi-antenna UEs, and the ARIS trajectory are optimized.
- In contrast to [24], our work considers mobile ARIS, where its trajectory is designed to minimize EMF exposure.
- A multi-variable optimization is formulated to reduce the average uplink exposure of the population while maintaining the QoS of all the users and taking into consideration the maximum transmit power of users, the maximum distance an ARIS can travel, and unique channel allocation for users.
- Solving optimization problem in its original form by jointly optimizing all the variables is complex due to its nature as a nonlinear fractional mixed-integer programming problem. To simplify the problem, we propose an alternate optimization (AO)-based algorithm where optimization variables are optimized alternately. Moreover, we assess the performance of the proposed scheme against other architectures, e.g., without RIS [23], with fixed RIS [24], and non-optimized RIS phases. We then conduct a complexity analysis of our algorithm and compare it with benchmark schemes.

The rest of the paper is structured as follows. Section II explains the considered system setup and signal model. Section III presents the problem formulation for minimizing the population's exposure. Subsequently, we present the proposed solution to the optimization problem. A comprehensive analysis of the algorithm's complexity is then provided. Simulation results are presented in Section IV. Lastly, Section V serves as the conclusion of the paper, encapsulating final remarks and interpretations.

### C. Notation and Organization

This paper uses the following notations. Lower-case (e.g.,  $x$ ), bold lower-case letter (e.g.,  $\mathbf{x}$ ), and bold upper-case letters (e.g.,  $\mathbf{X}$ ) denote scalars, vectors, and matrices, respectively. We use  $\mathbb{R}$  to denote set of real numbers and  $\mathbb{C}$  to denote the set of complex numbers while  $j$  represents the imaginary unit and  $\arg(\cdot)$  denotes the argument of a complex number. For a matrix  $\mathbf{a}$ ,  $\mathbf{a}^\top$  refers to its transpose, and  $\mathbf{a}^H$  refers to its conjugate transpose.

**TABLE I**  
SUMMARY OF NOTATIONS

Notation	Description
$\mathbf{G}$	Channel matrix between users and ARIS
$\mathbf{H}$	Channel matrix between ARIS and BS
$\mathbf{H}^d$	Direct channel matrix between users and BS
$\mathbf{H}$	Overall channel matrix between users and BS
$\Theta$	Phase-shift matrix of the RIS
$\mathbf{f}$	Transmit beamforming vector
$\mathbf{y}_u$	Received signal at the BS from user $u$
$\mathbf{s}$	Transmitted uplink signal
$\nu$	Additive white Gaussian noise at the BS
$\mathbf{p}$	Transmit power matrix
$\delta$	Resource allocation matrix
$(\alpha, \beta)$	Beamforming parameters
$\mathbf{Q}$	ARIS trajectory matrix
$\gamma_{uR}, \gamma_{uD}$	Sine of arrival and departure angles at the ARIS
$\eta_A, \eta_D$	Sine of arrival and departure angles at the BS
$d_{uR}, d_{RB}$	Distance between user and ARIS and between ARIS and BS respectively

The operator  $\text{diag}(\cdot)$  denotes the construction of a diagonal matrix based on an input vector, while  $\text{tr}(\cdot)$  denotes the trace of a matrix, and the operator  $\|\cdot\|$  represents the  $\ell_2$  norm. The notation  $\mathbf{A} \succeq 0$  indicates that the matrix  $\mathbf{A}$  is positive semidefinite. The optimal solution is denoted by  $(\cdot)^*$ .

## II. SYSTEM MODEL AND PROBLEM FORMULATION

In this section, we present the system setup, the signal, and the EMF exposure models. Then, we establish the problem formulation.

### A. System Setup and Signal Model

We consider an ARIS-assisted MU-MIMO network that consists of  $U$  uplink users. Each UE is equipped with  $M_t$  antennas, while the BS has  $M_r$  receiving antennas. We assume all the communicating nodes are equipped with uniform linear arrays (ULAs). In our scheme, the BS is located at the center of the cell, i.e.,  $\mathbf{q}_B = (x_B, y_B, h_B) = (0, 0, h_B)$ , while users are randomly distributed inside the cell at  $\mathbf{q}_u = (x_u, y_u, 0), \forall u \in \mathcal{U} \triangleq \{1, 2, \dots, U\}$ . As depicted in Fig. 1, the ARIS is a RIS deployed on a UAV flying at a fixed altitude  $h_0$ . Through the navigation of the UAV within the cell, the RIS reflects the signals received from the transmitters to the BS via  $N$  passive elements. For tractability, the flying duration of the UAV  $T$  is discretized into  $N_T$  time slots, each with duration  $\Delta = T/N_T$ . Consequently, the UAV trajectory is approximated by the sequence  $\mathbf{Q} = \{\mathbf{q}[\ell], \forall \ell \in \mathcal{N}_T\}$ , where

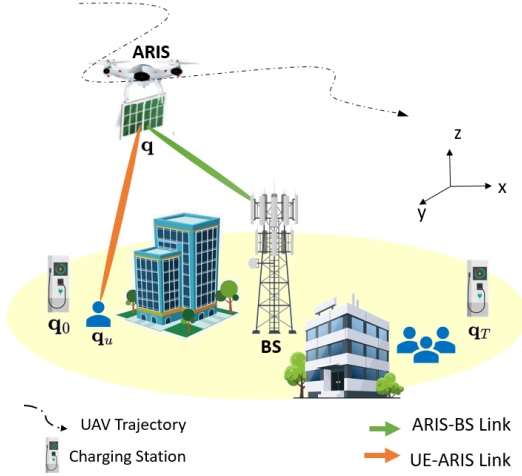


Fig. 1. ARIS-assisted network.

$\mathbf{q}[\ell] = (x[\ell], y[\ell], h_0), \forall \ell \in \mathcal{N}_{\mathcal{T}} \triangleq \{1, 2, \dots, N_{\mathcal{T}}\}$ . In addition, the maximum distance of one time slot is  $D_{\max} = \Delta V_{\max}$ , where  $V_{\max}$  denotes the maximum speed. The UAV flies from an initial location  $\mathbf{q}_0 = (x_0, y_0, h_0)$  to a final location  $\mathbf{q}_T = (x_T, y_T, h_0)$  during the considered flying duration before needing to be recharged.

We consider a multi-carrier system with  $N_c$  sub-channels. Hence, the channel between user  $u$  and the ARIS through the subcarrier  $n$ ,  $\mathbf{G}_{u,n}[\ell] \in \mathbb{C}^{N \times M_t}$ , can be modeled as a Rician channel, as the paths involving ARIS usually have a LoS component due to the high altitude of the UAV. At time slot  $\ell$ , the channel can be expressed as

$$\mathbf{G}_{u,n}[\ell] = \sqrt{\rho d_{uR}^{-\kappa_1}[\ell]} \tilde{\mathbf{G}}_{u,n}[\ell], \quad (1)$$

where

$$\tilde{\mathbf{G}}_{u,n}[\ell] = \sqrt{\frac{K_1}{K_1 + 1}} \mathbf{G}_{u,n}^{\text{LoS}}[\ell] + \sqrt{\frac{1}{K_1 + 1}} \mathbf{G}_{u,n}^{\text{NLoS}}[\ell]. \quad (2)$$

Here,  $\rho$  accounts for the received power from this path at the reference distance (1m),  $\kappa_1$  is the path-loss exponent,  $K_1$  denotes the Rician factor of the channel, and  $d_{uR}[\ell] = \|\mathbf{q}_u - \mathbf{q}[\ell]\|$  is the distance between the user  $u$  and the RIS. Meanwhile, the LoS and non line-of-sight (NLoS) channel components are defined as  $\mathbf{G}_{u,n}^{\text{LoS}}[\ell]$  and  $\mathbf{G}_{u,n}^{\text{NLoS}}[\ell]$ , where all elements of  $\mathbf{G}_{u,n}^{\text{NLoS}}[\ell]$  are independent and identically distributed (i.i.d) complex Gaussian random variables with zero mean and unit variance. However, the matrix  $\mathbf{G}_{u,n}^{\text{LoS}}[\ell]$  is expressed as

$$\mathbf{G}_{u,n}^{\text{LoS}}[\ell] = \mathbf{a}(N, \gamma_{uR}[\ell]) \mathbf{a}^H(M_t, \gamma_{uD}[\ell]), \quad (3)$$

where  $\mathbf{a}$  denotes the steering vector,  $\gamma_{uR}[\ell] = \frac{y_u - y[\ell]}{d_{uR}[\ell]}$  and  $\gamma_{uD}[\ell] = \frac{y_u - y[\ell]}{d_{uR}[\ell]}$  are the sine of the arrival

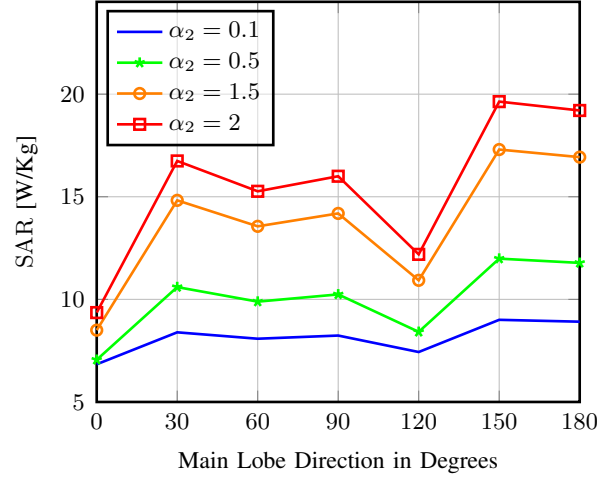


Fig. 2. SAR as a function of the main lobe direction.

and departure angles at the ARIS, respectively. The steering vector  $\mathbf{a}$  is a function of the number of antennas  $M$  and the sine of the angle between the transmitter and the receiver  $\gamma$ , i.e.,

$$\mathbf{a}(M, \gamma) \triangleq [1, e^{-j\frac{2\pi}{\lambda}d\gamma}, \dots, e^{-j\frac{2\pi}{\lambda}d(M-1)\gamma}]^T, \quad (4)$$

where  $\lambda$  is the wavelength and  $d$  the inter-antenna spacing [35]. Similarly, we define the channel between the RIS and BS through the RE  $n$  as follows

$$\mathbf{H}_n[\ell] = \sqrt{\rho d_{\text{RB}}^{-\kappa_2}[\ell]} \bar{\mathbf{H}}_n[\ell], \quad (5)$$

where

$$\bar{\mathbf{H}}_n[\ell] = \sqrt{\frac{K_2}{K_2 + 1}} \mathbf{H}_n^{\text{LoS}}[\ell] + \sqrt{\frac{1}{K_2 + 1}} \mathbf{H}_n^{\text{NLoS}}[\ell], \quad (6)$$

with  $\kappa_2$  as the path-loss exponent of the channel,  $K_2$  the Rician factor and  $d_{\text{RB}}[\ell] = \|\mathbf{q}_B - \mathbf{q}[\ell]\|$  the distance between the ARIS and the BS at  $\ell$  time. The matrix  $\bar{\mathbf{H}}_n[\ell] = \mathbf{a}(M_r, \eta_D[\ell]) \mathbf{a}^H(N, \eta_A[\ell])^H$ , represents the LoS component of the channel, depending on the sine of the arrival angle  $\eta_A[\ell] = (x_B - x[\ell])/d_{\text{RB}}[\ell]$ , and the departure angle  $\eta_D[\ell] = (x_B - x[\ell])/d_{\text{RB}}[\ell]$ . Each element of the NLoS component  $\mathbf{H}_n^{\text{NLoS}}[\ell]$  is i.i.d complex Gaussian distribution with zero mean and unit variance. For the direct link between the users and the BS, we consider a scenario where there is no direct LoS, i.e., the Rician factor goes to zero. Therefore, we define  $\mathbf{H}_{u,n}^{\text{d}} \in \mathbb{C}^{M_r \times M_t}$  as the NLoS channel between the user  $u$  and the BS via the  $n^{\text{th}}$  subcarrier, which can be modeled as Rayleigh fading channel with variance  $(\rho_1 d_{uB}^{-\kappa})$ .

The phase-shift matrix of the RIS is defined as  $\Theta[\ell] = \text{diag}(\boldsymbol{\theta}[\ell])$ , where  $\boldsymbol{\theta}[\ell] \triangleq [e^{j\theta_1[\ell]}, \dots, e^{j\theta_N[\ell]}]$  and  $\theta_i[\ell]$  is the induced shift by the RIS element  $i$ ,  $i \in \mathcal{N} \triangleq \{1, 2, \dots, N\}$ . The signal transmitted

from the user  $u$  to the BS via the subcarrier  $n$  at  $\ell$  time is expressed as  $\mathbf{s}_{u,n}[\ell] = \sqrt{p_{u,n}[\ell]} \mathbf{f}_{u,n}[\ell] x_{u,n}[\ell]$ , where  $x_{u,n}[\ell]$  is power-normalized transmitted information symbol and  $\mathbf{f}_{u,n}[\ell] \in \mathbb{C}^{M_t \times 1}$  is the beamforming vector at user  $u$ . Therefore, the received signal at the BS from user  $u$  at time slot  $\ell$  can be written as

$$\mathbf{y}_u[\ell] = \sum_{n=1}^{N_c} \delta_{u,n}[\ell] \mathbf{H}_{u,n}[\ell] \mathbf{s}_{u,n}[\ell] + \boldsymbol{\nu}[\ell], \forall u \in \mathcal{U}, \quad (7)$$

where  $\mathbf{H}_{u,n}[\ell] = \mathbf{H}_n[\ell] \boldsymbol{\Theta}[\ell] \mathbf{G}_{u,n}[\ell] + \mathbf{H}_{u,n}^d[\ell]$  denotes the overall channel matrix,  $\delta_{u,n}[\ell]$  is a binary RE allocation indicator, i.e.,  $\delta_{u,n}[\ell] = 1$  if the  $n^{\text{th}}$  RE is assigned to user  $u$  and zero otherwise, and  $\boldsymbol{\nu}$  represents the additive white Gaussian noise (AWGN) at the BS antennas with elements drawn from a zero-mean complex Gaussian distribution with variance  $\sigma^2$ .

In the considered scenario, the achievable rate of the user  $u$  using RE  $n$  is given by

$$r_{u,n}(\boldsymbol{\Gamma}[\ell]) = \omega \delta_{u,n}[\ell] \log_2 \left( 1 + \frac{p_{u,n}[\ell]}{\sigma^2} \gamma(\boldsymbol{\Gamma}_{u,n}[\ell]) \right), \quad (8)$$

where  $\omega$  denotes the bandwidth of each RE and  $\boldsymbol{\Gamma} \triangleq (\boldsymbol{\delta}, \mathbf{P}, \boldsymbol{\alpha}, \boldsymbol{\beta}, \boldsymbol{\theta}, \mathbf{Q})$  represents all system parameters over all subcarriers for all time slots. Specifically,  $\boldsymbol{\delta}$  represents the resource allocation for all users,  $\mathbf{P}$  denotes the transmit power allocation matrix for all users,  $(\boldsymbol{\alpha}, \boldsymbol{\beta})$  is the beamforming parameters for all users, and  $\boldsymbol{\theta}$  is the RIS phase-shift matrix over all time frame. Thus, the channel gain is given by

$$\begin{aligned} \gamma(\boldsymbol{\Gamma}_{u,n}[\ell]) &= \mathbf{f}_{u,n}^H[\ell] \mathbf{K}_{u,n}[\ell] \mathbf{f}_{u,n}[\ell] \\ &= \sum_{i=1}^{M_t} \alpha_{u,n,i}[\ell] k_{u,n,i,i}[\ell] + 2 \sum_{i=1}^{M_t} \sum_{j=i+1}^{M_t} \|k_{u,n,i,j}[\ell]\| \end{aligned} \quad (9)$$

$$\times \sqrt{\alpha_{u,n,i}[\ell] \alpha_{u,n,j}[\ell]}$$

$$\times \cos(\beta_{u,n,j}[\ell] - \beta_{u,n,i}[\ell] + \arg\{k_{u,n,i,j}[\ell]\}),$$

where  $\mathbf{K}_{u,n}[\ell] = \mathbf{H}_{u,n}^H[\ell] \mathbf{H}_{u,n}[\ell]$ . In (9),  $k_{u,n,i,j}[\ell]$  denotes the element in the  $i^{\text{th}}$  row  $j^{\text{th}}$  column of  $\mathbf{K}_{u,n}[\ell]$ . Meanwhile, the vector  $\mathbf{f}_{u,n}$  can be expressed as

$$\begin{aligned} \mathbf{f}_{u,n}(\boldsymbol{\alpha}_u[\ell], \boldsymbol{\beta}_u[\ell]) &= [\alpha_{u,n,1}[\ell] e^{j\beta_{u,n,1}[\ell]}, \\ &\dots, \alpha_{u,n,M_t}[\ell] e^{j\beta_{u,n,M_t}[\ell]}]^\top \in \mathbb{C}^{M_t \times 1} \end{aligned} \quad (10)$$

where  $\boldsymbol{\alpha}_u[\ell]$  denotes the power share between antennas and  $\boldsymbol{\beta}_u[\ell]$  represents the phase difference between them. Based on (8), the achievable rate of user  $u$  over all assigned subcarriers can be expressed as follows

$$r_u(\boldsymbol{\Gamma}[\ell]) = \sum_{n=1}^{N_c} r_{u,n}(\boldsymbol{\Gamma}[\ell]). \quad (11)$$

## B. Exposure Model

In practical uplink wireless communications, the SAR is generally used as a metric to evaluate the exposure, which is defined as the power absorbed by the human tissue per unit mass [14]. Hence, EMF-efficient communication networks are those endowed with low SAR while having a satisfactory QoS.

For a single-antenna UE, the SAR is directly proportional to the transmit power such that

$$\text{SAR}_u[\ell] = p_u[\ell] \overline{\text{SAR}} \text{ [W/Kg]}, \quad (12)$$

where  $p_u$  is the transmit power of user  $u$ , and  $\overline{\text{SAR}}$  [1/Kg] is the induced reference SAR when the transmit power is unity. The reference SAR depends on the antenna type of UE, the frequency of operation, the user's posture, etc. [36].

However, in the case of multi-antenna UE, the relation between the SAR and transmit power is not straightforward due to the coupling between the antennas and the user's body. Therefore, the relative share of power and the consideration of the phase shift between antennas can have a significant effect on the SAR level [21]. Notably, when examining a user device with  $M_t$  planar inverted F antennas (PIFA), the SAR is expressed as a function of the transmit beamforming parameters as follows

$$\text{SAR}_{u,n}[\ell] = p_{u,n}[\ell] \overline{\text{SAR}}(\boldsymbol{\alpha}_{u,n}[\ell], \boldsymbol{\beta}_{u,n}[\ell]), \quad (13)$$

where  $\boldsymbol{\alpha}_{u,n}[\ell] \in \mathbb{R}_+^{1 \times M_t}$  and  $\boldsymbol{\beta}_{u,n}[\ell] \in \mathbb{R}^{1 \times M_t}$  are vectors containing the relative power share and phase difference between the antenna ports of the  $u^{\text{th}}$  UE, respectively [21]. More precisely, the vector  $\boldsymbol{\alpha}_{u,n}$  is defined as  $\boldsymbol{\alpha}_{u,n}[\ell] \triangleq [\alpha_{u,n,1}[\ell], \dots, \alpha_{u,n,M_t}[\ell]]$  where  $\alpha_{u,n,i}[\ell] \triangleq \sqrt{p_{u,n,i}[\ell]} / \sqrt{p_{u,n,1}[\ell]}, \forall i \in \{1, \dots, M_t\}$ , represents the relative share of transmit power of the  $i^{\text{th}}$  antenna with respect to that of the first antenna. In this paper, we consider a worst-case scenario based on talk position where the UE is positioned 5 mm away from a phantom head model with realistic heterogeneous dielectric properties [21].

For a UE equipped with two PIFA antennas, i.e.,  $M_t = 2$ , the induced reference SAR is given by

$$\begin{aligned} \overline{\text{SAR}}(\boldsymbol{\alpha}_{u,n}[\ell], \boldsymbol{\beta}_{u,n}[\ell]) &= b_1 \alpha_{u,n,1}[\ell] + b_2 \sqrt{\alpha_{u,n,1}[\ell] \alpha_{u,n,2}[\ell]} \\ &+ b_3 \alpha_{u,n,2}[\ell] + \left( b_4 \alpha_{u,n,1}[\ell] + b_5 \sqrt{\alpha_{u,n,1}[\ell] \alpha_{u,n,2}[\ell]} \right. \\ &\left. + b_6 \alpha_{u,n,2}[\ell] \right) \times \sum_{i=7}^{13} b_i \cos((i-7)\beta_{u,n,2}[\ell] + b_{i+7}), \end{aligned} \quad (14)$$

where the parameters in  $\mathbf{b} = [b_1, b_2, \dots, b_{20}]$  are chosen to fit SAR values derived from the simula-

tion of SAR distribution within the phantom head [21]. Hence, we can see from (14) that the SAR depends directly on the relative power and the phase shift of the signal passed to different antennas. Typically, these values are designed to shape the antenna pattern and beamform the signal towards a specific direction. Therefore, the beamforming angle will have an indirect impact on the exposure. To illustrate this phenomenon, we show in Fig. 2 the induced SAR as a function of the direction of the main lobe of the antenna array. We can see that designing  $\alpha$  and  $\beta$  to achieve a specific direction of the main antenna array lobe can have a significant impact on the induced SAR, emphasizing the necessity of considering these parameters in the design of EMF-aware uplink multiple-input multiple-output (MIMO) systems. For a multi-carrier system, we quantify the individual exposure of user  $u$  by the total SAR over all subcarriers as follows

$$E_u(\mathbf{\Gamma}[\ell]) = \sum_{n=1}^{N_c} \delta_{u,n}[\ell] p_{u,n}[\ell] \overline{\text{SAR}}(\alpha_{u,n}[\ell], \beta_{u,n}[\ell]), \quad (15)$$

where  $\mathbf{\Gamma}[\ell]$  denote the system parameters at  $\ell$  time. Based on the per-user exposure at a specific time slot, we define the average uplink exposure across all the users as the mean value of the uplink EMF exposure levels experienced by individual users in the network over time, as follows [33]

$$I(\mathbf{\Gamma}) \triangleq \frac{\Delta}{N_T U} \sum_{\ell=1}^{N_T} \sum_{u=1}^U E_u(\mathbf{\Gamma}[\ell]) \text{ [W/Kg]}. \quad (16)$$

As shown in (16), the exposure is presented as a function of all the system variables which can be efficiently exploited to have an EMF-aware design. The dependence on these parameters provides various degrees of freedom that can be leveraged to reduce the exposure level.

In summary, the EMF exposure, especially for multi-antenna UE, relies on both UE transmit power and reference SAR value which depends on the antenna configuration. The interplay of  $\alpha$  and  $\beta$  along with transmit power highlights the importance of incorporating these factors into EMF-aware MIMO system design, promoting safer and more efficient communication networks.

### C. Problem Formulation

We investigate a strategy design for the ARIS-assisted multi-user MIMO uplink transmission with reduced EMF exposure, where we aim to optimize the parameters  $\mathbf{\Gamma}$  while maintaining the QoS for all the network users in terms of the required uplink

data rate. Considering the relevant constraints, our optimization problem can be formulated as follows

$$(P2) \quad \underset{\mathbf{\Gamma}}{\text{minimize}} \quad I(\mathbf{\Gamma}), \quad (17a)$$

subject to:

$$r_u(\mathbf{\Gamma}[\ell]) \geq \bar{R}_u, \quad \forall u \in \mathcal{U}, \forall \ell \in \mathcal{N}_T, \quad (17b)$$

$$\sum_{u=1}^U \delta_{u,n}[\ell] \leq 1, \quad \forall n \in \mathcal{N}_c, \forall \ell \in \mathcal{N}_T, \quad (17c)$$

$$|\theta_i[\ell]| = 1, \quad \forall i \in \mathcal{N}, \forall \ell \in \mathcal{N}_T, \quad (17d)$$

$$\sum_{n=1}^{N_c} \delta_{u,n}[\ell] p_{u,n}[\ell] \leq P_{\max}, \quad \forall u \in \mathcal{U}, \forall \ell \in \mathcal{N}_T, \quad (17e)$$

$$\|\mathbf{q}[\ell+1] - \mathbf{q}[\ell]\|^2 \leq D_{\max}^2, \quad 1 \leq \ell \leq N_T - 1, \quad (17f)$$

$$\mathbf{q}[1] = \mathbf{q}_0, \quad \mathbf{q}[N_T] = \mathbf{q}_T. \quad (17g)$$

The constraint (17b) ensures that each user  $u$  satisfies his required data rate  $\bar{R}_u$  and the constraint (17e) assures that the transmit power of each user  $u$  is below the maximum supported transmit power  $P_{\max}$ . Meanwhile, the RE allocation constraint presented in (17c) ensures that any RE can only be allocated to one user at a time. Furthermore, the constraints (17f) regulate the distance between two consecutive locations on the trajectory to be below the maximum distance that the ARIS can fly within a time slot  $D_{\max}$ . Further, the constraint (17g) specifies the initial and final locations for the UAV as  $\mathbf{q}_0$  and  $\mathbf{q}_T$ , respectively.

Note that it is difficult to directly tackle (P1) due to the introduction of the multi-antenna SAR model. More specifically, in our scheme, the optimization of the EMF exposure can not be simplified into a traditional power allocation problem. Additionally, the non-convex and discrete constraints, (17b), (17c), and (17d), further complicate the joint optimization.

## III. PROPOSED ALGORITHM FOR EMF-EFFICIENT MU-MIMO NETWORK WITH ARIS

Due to the coupling of the optimization variables, it is complicated to optimize the set of variables  $\mathbf{\Gamma}$  jointly, especially with high dimensional parameters and non-convex constraints. To reduce complexity, we apply the AO method, which is an iterative approach optimizing one variable while fixing the other variables alternately.

### A. MIMO Parameters Optimization

In this subsection, we optimize the MIMO parameters  $\alpha$  and  $\beta$ . It is worth noting that the beamforming vectors designed at a specific time instant are independent of those designed at different time

slots and from those of other users. Therefore, we solve this subproblem by optimizing the individual exposure at each time slot for each user separately.

Suppose the RE allocation vector  $\delta$ , phase-shift matrix  $\Theta$  and ARIS location  $\mathbf{q}$  are fixed in the feasible set that satisfies the corresponding constraints. At time  $\ell$ , the problem minimizing the exposure with respect to (w.r.t) relative power share  $\alpha_u$  and antenna shift  $\beta_u$  between the antennas ports of UE  $u$  is formulated as follows

$$(P2) \quad \underset{\alpha_u, \beta_u}{\text{minimize}} \quad E_u(\Gamma[\ell]), \forall \ell \in \mathcal{N}_T, \forall u \in \mathcal{U}, \quad (18a)$$

$$\text{subject to} \quad (17b). \quad (18b)$$

However, to initialize our AO iterative algorithm, we assume that all the users achieve their minimum required rate. By making this assumption, we ensure that the QoS constraint (17b) is satisfied. Additionally, we assume an equal share of data rate among subcarriers, which translates to an equal power distribution among the allocated subcarriers, which is not necessarily the optimal power allocation. These initial assumptions ensure the feasibility of the problem. Subsequently, the optimal distribution of required rates across subcarriers is determined by computing the optimal power allocation for each subcarrier to achieve an EMF-efficient power control mechanism in Sec. III-D. More in detail, the minimum transmit power that satisfies the rate constraint can be written from (8) and (17b) as

$$p_{u,n}(\Gamma_{u,n}) = (2^{\bar{r}_{u,n}/w} - 1) \frac{\sigma^2}{\gamma(\Gamma_{u,n})}, \quad (19)$$

where  $\bar{r}_{u,n}$  is the minimum required data rate through the  $n^{\text{th}}$  subcarrier. For notation convenience, we remove the dependency on time from the notation. Substituting (19) into the expression of the exposure, we get

$$E_u(\Gamma) = \sum_{n=1}^{N_c} \delta_{u,n} (2^{\bar{r}_{u,n}/w} - 1) \frac{\sigma^2 \overline{\text{SAR}}(\alpha_{u,n}, \beta_{u,n})}{\gamma(\Gamma_{u,n})}. \quad (20)$$

For a predefined  $\bar{r}_{u,n}$ , the beamforming parameters over different subchannels are independent of each other. Hence, the problem is equivalent to separately minimizing the ratio presented in (20) for each RE  $n$  as follows

$$\underset{\alpha_{u,n}, \beta_{u,n}}{\text{minimize}} \quad \delta_{u,n} \sigma^2 (2^{\bar{r}_{u,n}/w} - 1) \frac{\overline{\text{SAR}}(\alpha_{u,n}, \beta_{u,n})}{\gamma(\Gamma_{u,n})} \quad (21a)$$

$$\text{subject to} \quad \alpha_{u,n} \in \mathbb{R}_+^{M_t \times 1}, \quad (21b)$$

$$\beta_{u,n} \in \mathbb{R}^{M_t \times 1}. \quad (21c)$$

The formulated problem is a non-convex single-ratio programming. Therefore, we consider the Dinkelbach technique to decouple the denominator and nominator [37]. This method converts the ratio into a linear parameterized expression, which is then

---

### Algorithm 1: EMF Exposure-Aware Beamforming Design

---

- 1: Initialize  $\lambda^{(0)}$ , iteration index  $i = 0$ , convergence threshold  $\epsilon_1 \geq 0$ .
  - 2: **repeat**
  - 3: Calculate  $(\alpha_{u,n}^*, \beta_{u,n}^*)^{(i)}$  by solving (22).
  - 4: Update  $\lambda^{(i+1)}$  according to Eq. (24).
  - 5: Set  $i = i + 1$ .
  - 6: **until**  $|\lambda^{(i)} - \lambda^{(i-1)}| \leq \epsilon_1$ .
- 

optimized iteratively, where the slack parameter  $\lambda$  is updated at each iteration until convergence. At each iteration  $i$ , we solve the following problem

$$\underset{\alpha_{u,n}, \beta_{u,n}}{\text{minimize}} \quad f_1(\alpha_{u,n}, \beta_{u,n}, \lambda^{(i)}) \quad (22a)$$

$$\text{subject to} \quad \alpha_{u,n} \in \mathbb{R}_+^{M_t \times 1}, \quad (22b)$$

$$\beta_{u,n} \in \mathbb{R}^{M_t \times 1}, \quad (22c)$$

where the objective function depends on the slack variable  $\lambda^{(i)}$  as follows

$$f_1(\alpha_{u,n}, \beta_{u,n}, \lambda^{(i)}) = \delta_{u,n} \left( \sigma^2 (2^{\bar{r}_{u,n}/w} - 1) \right) \quad (23)$$

$$\overline{\text{SAR}}(\alpha_{u,n}, \beta_{u,n}) - \lambda^{(i)} \gamma(\Gamma_{u,n}),$$

and  $\lambda^{(i)}$  is updated as

$$\lambda^{(i)} = \delta_{u,n} \sigma^2 (2^{\bar{r}_{u,n}/w} - 1) \frac{\overline{\text{SAR}}(\alpha_{u,n}^{*(i-1)}, \beta_{u,n}^{*(i-1)})}{\gamma(\Gamma_{u,n}^{*(i-1)})}. \quad (24)$$

The solution of this subproblem is detailed in the iterative Algorithm 1, which guarantees the convergence to an optimal solution. The complexity of the proposed algorithm is with the order of  $\mathcal{O}(\sqrt{2M_t} - 2)$ .

### B. RIS Phase-shift Vector Design

Consider the optimization variables being fixed, the optimization of (P1) w.r.t the RIS vector  $\theta$  is formulated as

$$(P3) \quad \underset{\theta \in \mathbb{C}^{N \times 1}}{\text{minimize}} \quad \sum_{u=1}^U \sum_{n=1}^{N_c} \delta_{u,n} \frac{\sigma^2 (2^{\bar{r}_{u,n}/w} - 1) \overline{\text{SAR}}_{u,n}}{\gamma(\Gamma_{u,n})} \quad (25a)$$

$$\text{subject to} \quad (17d). \quad (25b)$$

It is worth noting that the phase shifts of the ARIS are designed only to assist the uplink transmission for users within the considered cell. To simplify the notation, let  $\overline{\text{SAR}}_{u,n}$  denote  $\overline{\text{SAR}}(\alpha_{u,n}, \beta_{u,n})$ . Due to the non-convex nature of the problem, which arises from its formulation as a sum-of-ratios problem, we employ the quadratic transform technique to reformulate it [37]. This technique aims to recast the non-convex sum of fractions problem as a sequence of convex problems that can be efficiently

solved. As such, the problem can be reformulated as

$$(P3) \quad \underset{\boldsymbol{\theta}, \mathbf{y}}{\text{minimize}} \quad f_2(\boldsymbol{\theta}, \mathbf{y}) \quad (26a)$$

$$\text{subject to} \quad (17d), \quad (26b)$$

where the new objective function is expressed as

$$f_2(\boldsymbol{\theta}, \mathbf{y}) \triangleq \sum_{u=1}^U \sum_{n=1}^{N_c} \delta_{u,n} (2 y_{u,n} c_{u,n} - y_{u,n}^2 \gamma(\boldsymbol{\Gamma}_{u,n})), \quad (27)$$

and

$$c_{u,n} \triangleq \sqrt{\sigma^2 (2^{\bar{r}_{u,n}/w} - 1) \overline{\text{SAR}}_{u,n}}. \quad (28)$$

Here,  $\mathbf{y} = [y_{1,1}, \dots, y_{u,n}, \dots, y_{U,N}]$  refers to the vector of auxiliary variables. Resorting to the AO method, we address the new formulated problem by iteratively optimizing the introduced variables in  $\mathbf{y}$ . The optimal value for  $\mathbf{y}$  is obtained by solving  $\partial f_2(\boldsymbol{\theta}, \mathbf{y}) / \partial \mathbf{y} = 0$ , while fixing  $\boldsymbol{\theta}$  as follows

$$y_{u,n}^* \triangleq \frac{c_{u,n}}{\gamma(\boldsymbol{\Gamma}_{u,n})}. \quad (29)$$

Subsequently, the objective function can be written as

$$f_2(\boldsymbol{\theta}, \mathbf{y}) = \sum_{u=1}^U \sum_{n=1}^{N_c} \delta_{u,n} m_{u,n} - \delta_{u,n} y_{u,n}^2 \|\mathbf{H}_n \boldsymbol{\Theta} \mathbf{g}_{u,n} + \mathbf{h}_{u,n}^d\|^2, \quad (30)$$

where  $m_{u,n} = 2y_{u,n}c_{u,n}$ ,  $\mathbf{g}_{u,n} \triangleq \mathbf{G}_{u,n} \mathbf{f}_{u,n}$  and  $\mathbf{h}_{u,n}^d \triangleq \mathbf{H}_{u,n}^d \mathbf{f}_{u,n}$ . To solve this problem optimizing RIS phase shifts while fixing  $\mathbf{y}$ , we use the matrix lifting technique [38]. First, we rewrite the objective function differently as follows

$$f_2(\boldsymbol{\theta}, \mathbf{y}) = \sum_{u=1}^U \sum_{n=1}^{N_c} \delta_{u,n} m_{u,n} - \delta_{u,n} y_{u,n}^2 (\boldsymbol{\theta}^H \mathbf{A}_{u,n} \boldsymbol{\theta} + 2\text{Re}\{\boldsymbol{\theta}^H \mathbf{b}_{u,n}\}), \quad (31)$$

where  $\mathbf{A}_{u,n} \triangleq \text{diag}(\mathbf{g}_{u,n})^H \mathbf{H}_n^H \mathbf{H}_n \text{diag}(\mathbf{g}_{u,n})$ , and  $\mathbf{b}_{u,n} \triangleq \text{diag}(\mathbf{g}_{u,n})^H \mathbf{H}_n^H \mathbf{h}_{u,n}^d$ . By removing all the terms that do not depend on  $\boldsymbol{\theta}$ , we can write the optimization problem for fixed  $\mathbf{y}$  as

$$\underset{\boldsymbol{\theta}}{\text{minimize}} \quad -\boldsymbol{\theta}^H \mathbf{R} \boldsymbol{\theta} \quad (32a)$$

$$\text{subject to} \quad |\theta_i| = 1, \forall i = \{1, \dots, N+1\}. \quad (32b)$$

Here, the matrix  $\mathbf{R}$  is defined as  $\mathbf{R} \triangleq \begin{bmatrix} \mathbf{A} & \mathbf{b} \\ \mathbf{b}^H & 0 \end{bmatrix}$ ,

where

$$\begin{aligned} \mathbf{A} &\triangleq \sum_{u=1}^U \sum_{n=1}^{N_c} \delta_{u,n} y_{u,n}^2 \mathbf{A}_{u,n}, \\ \mathbf{b} &\triangleq \sum_{u=1}^U \sum_{n=1}^{N_c} \delta_{u,n} y_{u,n}^2 \mathbf{b}_{u,n}. \end{aligned} \quad (33)$$

The reformulated problem is non-convex quadratically constrained quadratic problem (QCQP) due to the unit modulus constraint. Thus, we proceed by using the matrix lifting technique to reformulate (32) as a rank-one optimization problem and we

---

### Algorithm 2: EMF Exposure-Aware RIS Phase Shifts Design

---

- 1: Initialize  $\mathbf{y}^{(0)}$ , set iteration index  $i = 0$ , number of Gaussian randomization  $I_{\text{GR}}$ , and convergence threshold  $\epsilon_2 \geq 0$ .
  - 2: **repeat**
  - 3:   Solve problem (P3') using SDR for fixed  $\mathbf{y}^{(I_2)}$ ,  $\bar{\boldsymbol{\Theta}}^*$ , and  $I_{\text{GR}}$ .
  - 4:   **for**  $k = 1, \dots, I_{\text{GR}}$
  - 5:     Generate a matrix with zero mean and  $\bar{\boldsymbol{\Theta}}^*$  variance:  $\boldsymbol{\eta}^k \doteq \mathcal{N}(0, \bar{\boldsymbol{\Theta}}^*)$ .
  - 6:     Construct the feasible vector as  $(\boldsymbol{\theta}^k)^* = \text{sgn}(\boldsymbol{\eta}^k)$ .
  - 7:   **End**
  - 8:   Determine the approximate solution of  $\boldsymbol{\theta}^* = \min_{\hat{\boldsymbol{\theta}}_i} \boldsymbol{\theta}_i^T \mathbf{R} \boldsymbol{\theta}_i$ .
  - 9:   Set  $i = i + 1$ .
  - 10:   Update  $\mathbf{y}^{(i)}$  according to Eq. (29).
  - 11: **until**  $|\mathbf{y}^{(i-1)} - \mathbf{y}^{(i)}| \leq \epsilon_2$ .
- 

rewrite the problem w.r.t the matrix  $\bar{\boldsymbol{\Theta}} = \bar{\boldsymbol{\theta}} \bar{\boldsymbol{\theta}}^H$ , where  $\bar{\boldsymbol{\theta}} = \begin{bmatrix} \boldsymbol{\theta} \\ 1 \end{bmatrix}$ . Let us rewrite (32) in terms of  $\bar{\boldsymbol{\Theta}}$  as

$$(P3') \quad \underset{\bar{\boldsymbol{\Theta}}}{\text{minimize}} \quad -\text{tr}(\mathbf{R} \bar{\boldsymbol{\Theta}}) \quad (34a)$$

$$\text{subject to} \quad \bar{\Theta}_{i,i} = 1, \forall i = \{1, \dots, N+1\}, \quad (34b)$$

$$\bar{\boldsymbol{\Theta}} \succeq 0. \quad (34c)$$

Considering that  $\bar{\boldsymbol{\Theta}}$  is a positive semi-definite matrix with each diagonal element equal to unity, we introduce the constraint (34b) and (34c). Now the problem is formulated as a standard convex semi-definite program (SDP) allowing us to relax the rank-one constraint and optimally solve it by an existing convex optimization solver such as CVX [39]. In general, a relaxed problem may not lead to a rank-one solution, which means that the obtained solution serves only as an upper bound of the optimal solution of the problem (P3'). Therefore, we use Gaussian randomization to construct a rank one matrix to the initial problem (P3) from the optimal solution of (P3'). Initially, we derive the eigenvalue decomposition of  $\boldsymbol{\Theta} = \mathbf{U} \mathbf{D} \mathbf{U}^H$  where  $\mathbf{U}$  is a unitary matrix and  $\mathbf{D} = \text{diag}(\lambda_1 \dots \lambda_{N+1})$  is a diagonal matrix, both with same size  $(N+1) \times (N+1)$ . Then, we have a first suboptimal solution for (P3') as  $\bar{\boldsymbol{\theta}} = \mathbf{U} \mathbf{D}^{\frac{1}{2}} \mathbf{r}$ , where  $\mathbf{r} \in \mathbb{C}^{(N+1) \times 1}$  is a random vector generated according to a circularly symmetric



complex Gaussian (CSCG) distribution with zero-mean and  $\mathbf{I}_{N+1}$  covariance matrix. Furthermore, we approximate the optimal solution of (P3) by generating independently random Gaussian vectors  $\mathbf{r}$ . Finally, we recover the solution  $\mathbf{v}$  based on  $\boldsymbol{\theta} = e^{j \arg\left(\frac{\bar{\boldsymbol{\theta}}}{\bar{\boldsymbol{\theta}}_{N+1}}\right)}$ . It has been proved that following the semi-definite relaxation (SDR) approach by a sufficiently large number of randomization of  $\mathbf{r}$  guarantees an  $\frac{\pi}{4}$ -approximation of the optimal objective function value of the initial problem [38]. Regarding the complexity of the proposed solution, it is worth noting that SDP is typically solved using the interior point method which yields an  $\epsilon$ -optimal solution. Hence, by reserving the term with highest order and assuming perfect channel state information (CSI), the complexity of the proposed solution is  $\mathcal{O}(N^{3.5})$ .<sup>1</sup>

### C. RE Allocation Optimization

Finding the optimal number of allocated subcarriers to each user is essential to reduce the overall exposure effectively. It is worth noting that the allocation of multiple subcarriers to a single user has a remarkable effect of diminishing the necessary transmission power, and consequently reducing the individual exposure (15). In this regard, for given RIS phase shifts, beamforming parameters, and ARIS trajectory, the resource allocation problem can be formulated as

$$(P4) \quad \underset{\boldsymbol{\delta} \in \mathbb{R}^{U \times N_c}}{\text{minimize}} \quad I(\boldsymbol{\Gamma}) \quad (35a)$$

$$\text{subject to} \quad (17e), (17c). \quad (35b)$$

This subproblem is a constrained binary non-convex problem which is challenging to solve. Therefore, we propose a heuristic algorithm for resource allocation. Initially, each user is allocated one RE, then, further subcarriers are assigned to the users with the highest expected EMF exposure, quantified by a proper metric. We establish a ranking metric designed to exhibit scaling laws analogous to those of the EMF exposure with respect to the required data rate and path-loss, i.e.,

$$\rho_u^{(i)} \triangleq (2^{r_u^{(i)}/w} - 1)(d_{uR}^{K_1} d_{RB}^{K_2}), \quad (36)$$

where  $r_u^{(i)} = r_u^*/N_u^{(i)}$  quantifying the rate achieved through the allocated subcarriers  $N_u^{(i)}$  which is updated at each iteration  $i$  of the algorithm. However, the total rate  $r_u^*$  is achieved through prior subproblems optimization which ensures that power

---

### Algorithm 3: EMF Exposure-Aware Resource Element Allocation

---

- 1: Initialize iteration index  $i = 1$ .
  - 2: Assign one RE to each user, i.e.,  $\mathcal{N}_u = \{u\}, \forall u \in \mathcal{U}$ .
  - 3: Define  $\mathcal{S}$  as the set of non-assigned subcarriers:  $\mathcal{S} = \{U + 1, \dots, N_c\}$ .
  - 4: **while**  $\mathcal{S} \neq \emptyset$
  - 5:   Solve  $u^* = \underset{u \in \mathcal{U}}{\text{argmax}} \left( \rho_u^{(i)} \right)$ .
  - 6:   Assign the first subcarrier from  $\mathcal{S}$  to user  $u^*$ , i.e.,  $\mathcal{N}_{u^*} = \mathcal{N}_{u^*} \cup \mathcal{S}(1)$ .
  - 7:   Update  $\delta_{u^*, \mathcal{S}(1)} = 1$ .
  - 8:   Remove the assigned subcarrier from  $\mathcal{S}$ , i.e.,  $\mathcal{S} = \mathcal{S} \setminus \mathcal{S}(1)$ .
  - 9: **end**
- 

remains within the maximum allowed budget constraint. Given the optimized variables alternately updated, we ensure that the power does not exceed the maximum allowed power limit. This metric is proportional to the EMF exposure which prioritizes users that have a high required rate and path-loss. At the  $i^{\text{th}}$  iteration, we assign a subcarrier to the user with the highest value of  $\rho_u^{(i)}$ . Then, we update the value of the metric and repeat the allocation process till all the remaining subcarriers are assigned to users, as detailed in Algorithm 3. The complexity of this algorithm is in the order of  $\mathcal{O}(N_c - U)$ .

### D. Power control

As we mentioned before, we initially assumed an equal distribution of transmit power among subcarriers to ensure feasibility and satisfy QoS constraints. However, this allocation may not be optimal. Therefore, a proper design for the power sharing between subcarriers is essential to minimize the exposure. Once we obtain the optimal power allocation, we update the data rate achieved at each subcarrier. Then, we solve other subproblem iteratively until convergence is reached. In the following, we consider the optimization of (P1) w.r.t the transmit power  $\mathbf{P}$  while holding the remaining optimization variables fixed. Given the independence of each user's transmit power, wherein each user can adjust their power level without influencing or being influenced by the power levels of other users, we proceed to optimize the power allocated to each user

<sup>1</sup>The channel estimation process in RIS-aided networks can be obtained based on existing methods, such as the techniques outlined in [40]–[42].

---

**Algorithm 4: EMF Exposure-Aware Power Allocation**


---

- 1: Initialize  $\mu^{(0)}$ ,  $\lambda^{(0)}$ , and the convergence threshold for Newton-Raphson algorithm
  - 2: Define  $\mathcal{L}$  using Eq. (55).
  - 3: Calculate  $\mu^*$  and  $\lambda^*$  solving Eq. (54) using Newton-Raphson algorithm.
  - 4: **for**  $n = 1, 2, \dots, N_c$
  - 5:   Calculate  $p_{u,n}^*$  using Eq. (38).
  - 6: **end**
- 

individually for different time slots as follows

$$(P5) \quad \underset{\mathbf{p}_u \in \mathbb{R}_+^{1 \times N_c}}{\text{minimize}} \quad \sum_{n=1}^{N_c} \delta_{u,n} \overline{\text{SAR}}_{u,n} p_{u,n} \quad (37a)$$

$$\text{subject to} \quad r_u(\mathbf{\Gamma}) \geq \bar{R}_u, \quad (37b)$$

$$\sum_{n=1}^{N_c} \delta_{u,n} p_{u,n} \leq P_{\max}. \quad (37c)$$

The subproblem (P5) is a convex nonlinear optimization problem w.r.t  $\mathbf{p}_u$  which can be solved using the KKT conditions. The expression of the optimal transmit power over the  $n^{\text{th}}$  subcarrier can be derived as

$$p_{u,n}^* = \max \left\{ \frac{\delta_{u,n} w \mu^*}{\ln(2)(\overline{\text{SAR}}_{u,n} + \lambda^*)} - \frac{\delta_{u,n} \sigma^2}{\gamma(\mathbf{\Gamma}_{u,n}^*)}, 0 \right\}, \quad (38)$$

$$\forall u \in \mathcal{U}, \forall n \in \mathcal{N}_c,$$

where  $\mu^*$  and  $\lambda^*$  are the Lagrangian multipliers obtained by solving the KKT equations. The details of the derivation can be found in Appendix A. The optimal power,  $p_{u,n}^*$ , allocated to each subcarrier determines the share of this subcarrier from the total required rate, i.e.,  $\bar{r}_{u,n}$  using (8), which is used for later iterations of the alternate optimization. Algorithm 4 outlines the proposed solution for power allocation over subcarriers.

The complexity of the transmit power allocation is primarily associated with the computational expense of calculating the Lagrangian multipliers. In our subproblem, the complexity of the proposed solution is based on solving a system of  $(N_u + 4)$  nonlinear equations. Hence, the complexity of Algorithm 4, optimizing the power for all users, is in the order of  $\mathcal{O} \left( \sum_{u=1}^U N_u^2 \right)$ .

### E. ARIS Trajectory Design

After solving the optimization variables  $(\alpha, \beta)$ , with  $\delta$ , and  $\mathbf{P}$ , problem (P1) regarding the opti-

mization target  $\mathbf{Q}$  is formulated as

$$(P6) \quad \underset{\mathbf{Q} \in \mathbb{R}^{2 \times N_T}}{\text{minimize}} \quad I(\mathbf{\Gamma}) \quad (39a)$$

$$\text{subject to} \quad (17f), (17g). \quad (39b)$$

Because of the non-convexity of the objective function (39a) and the constraint (17b),(17f), there exist great challenges to deal with (P6) directly. It can be observed that (P6) is a sum-of-ratio fractional programming. According to [37], (P6) is equivalent to a minimization problem formulated by

$$\underset{\mathbf{Q}, \mathbf{X}}{\text{minimize}} \quad f_4(\mathbf{Q}, \mathbf{X}) \quad (40a)$$

$$\text{subject to} \quad (17f), (17g), \quad (40b)$$

where

$$f_4(\mathbf{Q}, \mathbf{X}) \triangleq \sum_{\ell=1}^{N_T} \sum_{u=1}^U \sum_{n=1}^{N_c} \delta_{u,n}[\ell] 2 x_{u,n}[\ell] c_{u,n}[\ell] - \delta_{u,n}[\ell] x_{u,n}^2[\ell] \gamma(\mathbf{\Gamma}_{u,n}[\ell]). \quad (41)$$

The matrix  $\mathbf{X}[\ell] \in \mathbb{R}^{U \times N_c}$ ,  $\forall \ell \in \mathcal{N}_{\mathcal{T}}$ , is employed as an auxiliary variable. Note that (40) is minimized by iteratively updating  $\mathbf{Q}$  and  $\mathbf{X}$  until convergence. For a fixed  $\mathbf{Q}$ , the optimal  $x_{u,n}$  can be derived in closed-form as

$$x_{u,n}^*[\ell] = \frac{c_{u,n}[\ell]}{\gamma(\mathbf{\Gamma}_{u,n}^*[\ell])}, \forall u \in \mathcal{U}, \forall n \in \mathcal{N}_c \text{ and } \forall \ell \in \mathcal{N}_{\mathcal{T}}. \quad (42)$$

However, the new equivalent problem is still non-convex with respect to  $\mathbf{Q}$ . To show the dependency of the objective function on the ARIS location, we express  $\gamma(\mathbf{\Gamma}_{u,n}[\ell])$  differently as

$$\gamma(\mathbf{\Gamma}_{u,n}[\ell]) = \frac{a_{u,n}[\ell]}{d_{uR}^{\kappa_1}[\ell]} + \frac{b_{u,n}[\ell]}{\sqrt{d_{uR}^{\kappa_1}[\ell]} d_{RB}^{\kappa_2}[\ell]}, \quad (43)$$

where

$$a_{u,n}[\ell] = \rho^2 \|\bar{\mathbf{H}}_n[\ell] \Theta[\ell] \bar{\mathbf{G}}_{u,n}[\ell] \mathbf{f}_{u,n}[\ell]\|^2, \quad (44)$$

$$b_{u,n}[\ell] = 2 \rho \text{Re} \left\{ \mathbf{h}_{u,n}^d[\ell]^H \bar{\mathbf{H}}_n[\ell] \Theta[\ell] \bar{\mathbf{G}}_{u,n}[\ell] \mathbf{f}_{u,n}[\ell] \right\}, \quad (45)$$

and

$$\mathbf{h}_{u,n}^d[\ell] = \mathbf{H}_{u,n}^d[\ell] \mathbf{f}_{u,n}[\ell]. \quad (46)$$

It is noteworthy that the non-convexity of the subproblem comes from the coupling between the distances between users-ARIS and ARIS-BS. With this in mind, we intend to decouple the two variables and relax the problem by introducing new auxiliary variables  $\mathbf{U}$  and  $\mathbf{v}$ , which establish bounds on the distances. Specifically,  $\mathbf{U}$  bounds the distance between users and the ARIS, and  $\mathbf{v}$  bounds the distance between the ARIS and the BS as follows

$$u_u[\ell] \geq d_{uR}[\ell], \forall u \in \mathcal{U} \text{ and } \forall \ell \in \mathcal{N}_{\mathcal{T}}, \quad (47)$$

$$v[\ell] \geq d_{RB}[\ell], \forall \ell \in \mathcal{N}_{\mathcal{T}}. \quad (48)$$

Considering the new constraints, the optimization problem is reformulated as

$$\underset{\mathbf{Q}, \mathbf{U}, \mathbf{v}}{\text{minimize}} \quad f_4(\mathbf{Q}, \mathbf{X}) \quad (49a)$$

$$\text{subject to} \quad (17f), (17g), (47), (48), \quad (49b)$$

where the objective function is expressed as follows

$$f_5(\mathbf{Q}, \mathbf{X}, \mathbf{U}, \mathbf{v}) = \sum_{\ell=0}^{N_T} \sum_{u=1}^U \sum_{n=1}^{N_c} \delta_{u,n}[\ell] 2 x_{u,n}[\ell] c_{u,n}[\ell] - \delta_{u,n}[\ell] x_{u,n}^2[\ell] \left( \frac{a_{u,n}[\ell]}{u_u[\ell]^{\kappa_1} v[\ell]^{\kappa_2}} + \frac{b_{u,n}[\ell]}{u_u[\ell]^{\frac{\kappa_1}{2}} v[\ell]^{\frac{\kappa_2}{2}}} \right). \quad (50)$$

Note that the equality at the optimal solution between the original and the new reformulated subproblem is guaranteed since increasing the value of the new slack variables reduces the objective value. However, a minimization problem with a non-convex objective function and/or a non-convex feasible region is generally non-convex, and thus difficult to be solved optimally. Based on these facts, we propose an iterative algorithm to solve problem (49) by applying successive convex approximation (SCA) [43]. This approach relies mainly on the first-order Taylor series to linearise the non-convex objective function and constraints. Hence, for given initial points  $(\mathbf{U}^0, \mathbf{v}^0)$ , which are feasible to (49), we derive the first-order Taylor expansion of (47), (48), and (50) as detailed in Appendix V. The approximated problem is written as

$$\underset{\mathbf{Q}, \mathbf{U}, \mathbf{v}}{\text{minimize}} \quad \bar{f}_5(\mathbf{Q}, \mathbf{X}, \mathbf{U}, \mathbf{V}) \quad (51a)$$

$$\text{subject to} \quad (17f), (17g), (57), (58), \quad (51b)$$

where

$$\bar{f}_5(\mathbf{Q}, \mathbf{X}, \mathbf{U}, \mathbf{V}) = \sum_{\ell=1}^{N_T} \sum_{u=1}^U \sum_{n=1}^{N_c} \delta_{u,n}[\ell] 2x_{u,n}[\ell] c_{u,n}[\ell] - \delta_{u,n}[\ell] x_{u,n}^2[\ell] (A_{u,n}[\ell] + B_{u,n}[\ell]). \quad (52)$$

After approximation, the problem is convex which can be solved efficiently using convex solvers such as CVX. The ARIS trajectory design is detailed in Algorithm 5. However, it is difficult to generate an initial trajectory that satisfies all constraints. So, we initialize  $\mathbf{Q}^0$  as the direct trajectory between the given start and final locations. Based on  $\mathbf{Q}^0$ , we initialize also the auxiliary variables  $(\mathbf{U}^0, \mathbf{v}^0)$  introduced in the subproblem (P6'). This guarantees that we have feasible initial points to start the SCA algorithm [43]. Note that the complexity of the proposed algorithm relies on the SCA method and can be expressed as  $\mathcal{O}(N_v^{3.5})$ , where  $N_v = (3 + U)N_T$  is the number of optimization variables.

### F. Overall Algorithm

Now that we have studied the optimization of transmit beamforming parameters  $(\alpha, \beta)$ , transmit power  $\mathbf{P}$ , resource allocation vector  $\delta$ , ARIS phase-shift matrix and its trajectory  $\mathbf{Q}$ . In this section, we propose the overall EMF-aware algorithm and then analyze its complexity. By using the AO framework, the overall transmission scheme is detailed in Algo-

---

### Algorithm 5: EMF Exposure-Aware ARIS Trajectory Design

---

- 1: Initialize  $\mathbf{Q}^{(0)}, \mathbf{U}^{(0)}, \mathbf{v}^{(0)}, \mathbf{X}^{(0)}$ , iteration indices  $i = 0, k = 0$ , and convergence threshold  $\epsilon_5 \geq 0$ .
  - 2: **repeat**
  - 3:   **repeat**
  - 4:     Set feasible  $\mathbf{Q}_{\text{feas}}^{(k)}, \mathbf{U}_{\text{feas}}^{(k)}$ , and  $\mathbf{v}_{\text{feas}}^{(k)}$  using  $\mathbf{X}^{(i)}$ .
  - 5:     Update  $\mathbf{Q}^{(k+1)}, \mathbf{U}^{(k+1)}$  and  $\mathbf{v}^{(k+1)}$  by solving (P6).
  - 6:     Set  $k = k + 1$ .
  - 7:   **until** convergence.
  - 8:   Update  $\mathbf{X}^{(i+1)}$  according to Eq. (42) for given  $\mathbf{Q}^{*(i)}$ .
  - 9:   Set  $i = i + 1$ .
  - 10: **until**  $\|\mathbf{X}^{(i-1)} - \mathbf{X}^{(i)}\| \leq \epsilon_5$ .
- 

---

### Algorithm 6: Overall EMF Exposure-Aware Algorithm for UL MU-MIMO ARIS-Aided Network

---

- 1: Initialize  $\Gamma^{(0)}$ , iteration index  $i = 0$  and convergence threshold  $\epsilon$
  - 2: **repeat**
  - 3:   **for**  $\ell = 1, 2, \dots, N_T$
  - 4:     Calculate  $(\alpha[\ell], \beta[\ell])^{(i+1)}$  using Alg. 1
  - 5:     Calculate  $\theta[\ell]^{(i+1)}$  using Alg. 2
  - 6:     Calculate  $\delta[\ell]^{(i+1)}$  using Alg. 3
  - 7:     Calculate  $\mathbf{P}[\ell]^{(i+1)}$  using Alg. 4
  - 8:   **end**
  - 9:   Calculate  $\mathbf{Q}^{(i+1)}$  using Alg. 5
  - 10:   Set  $i = i + 1$ .
  - 11: **until**  $\left| I(\Gamma^{(i-1)}) - I(\Gamma^{(i)}) \right| \leq \epsilon$ .
- 

rithm 6. The complexity of each subproblem was derived separately. However, the overall complexity of Algorithm 6 mainly centers on two key steps: step (5) the RIS phase shifts design, and step (9) the ARIS trajectory optimization.

In conclusion, the overall complexity of the proposed solution by reserving the terms with the highest orders is expressed as  $\mathcal{O}(N_T N^{3.5} + N_v^{3.5})$ .

## IV. NUMERICAL RESULTS AND DISCUSSIONS

In this section, we present the numerical results obtained by Monte Carlo simulations for our setup. In the evaluation scenario, we assume that the

**TABLE II**  
SIMULATION PARAMETERS

Parameter	Description	Value
$U$	Number of users	8
$N$	Total number of channels	80
$N_c$	Number of subcarriers	80
$M_r$	Number of receive antennas	32
$M_t$	Number of transmit antennas	2
$h_b$	BS height	25 m
$h_0$	ARIS height [44]	100 m
$\Delta$	Time slot duration	15 s
$T$	Total flight duration	300 s
$V_{\max}$	Maximum velocity [45]	25 m/s
$w$	Bandwidth [46]	240 kHz
$\rho$	LoS path-loss [47]	-24.91 dB
$\rho_1$	NLoS path-loss [47]	-19.96 dB
$P_{\max}$	Maximum transmit power [46]	26 dBm
$\sigma^2$	Noise variance	-174 dBm/Hz
$f_c$	Carrier frequency [48]	700 MHz
$\kappa$	Path-loss exponent of UE-BS link [47]	3.908
$K_1 = K_2$	Rician factor of UE-ARIS and ARIS-BS links [45]	3 dB
$\kappa_1 = \kappa_2$	Path-loss exponent of UE-ARIS and ARIS-BS links [47]	2.2

users are uniformly distributed in a circle centered at the origin of the coordinate system, i.e., the BS location, with a radius of 100 m, i.e., the cell coverage. Additionally, we specified the first and final locations of the ARIS as,  $\mathbf{q}_0 = (-80, 55, 100)$  and  $\mathbf{q}_T = (100, 20, 100)$ , respectively. Note that the initial and final points of the ARIS trajectory can be selected arbitrarily, and they can even be the same point, e.g., the same charging station. We consider diverse requirements for the users with the considered rate threshold  $\bar{\mathbf{R}} = [10, 9.4, 8.5, 6.7, 4.5, 7.6, 8.7, 3.1]$  Mbps. Here, the path-losses experienced by the LoS and NLoS links are modeled using 3GPP Urban Micro (UMi) scenario from [47, Table B.1.2.1-1]. For convenience, the simulation parameters are summarized in Table II, unless otherwise specified. The optimization of the convex subproblems in this paper is solved using CVX Toolbox, which is a powerful tool for solving convex problems [39]. We compare the performance of our proposed algorithm with several benchmarks, i.e.,

- Without RIS [23]: We rely solely on the direct NLoS link between the UE and BS similar to [23] while being adopted to our setup. The complexity of this benchmark relies on the transmit power optimization. Hence, its com-

plexity is in the order of  $\mathcal{O}\left(\sum_{u=1}^U N_u^2\right)$ , where  $N_u$  is the number of allocated subcarriers allocated to each user  $u \in \mathcal{U}$ .

- Fixed Deployed RIS [24]: The RIS is deployed in a fixed place, i.e., hovering, similar to [24]. For fairness, we extend [24] from SIMO to MIMO and further optimize the location of the RIS to minimize  $I$  using the divide-and-conquer algorithm. The algorithm iteratively divides the search area into subregions, halving the search radius at each step until the optimal ARIS deployment location is identified. Additionally, we account for the time required for the ARIS to travel to and return from the deployment location. The complexity of this benchmark is in the order of  $\mathcal{O}(N_T N^{3.5})$ .
- ARIS with random phases: The proposed algorithm, but with random RIS phase shifts, is considered, where all variables are optimized except for the ARIS phases.
- ARIS with zero Phases: The proposed algorithm, but with zero RIS phase shifts, is considered, where all variables are optimized except for the ARIS phases.

#### A. Impact of ARIS Trajectory

In this section, we show the impact of the ARIS trajectory design on the exposure level in Fig. 3 and Table III. In Fig. 3, we compare three different trajectories for the UAV. One flying path is the proposed designed trajectory to minimize exposure where all the system parameters are optimized, i.e.,  $\hat{\Gamma}$ . The second trajectory is the direct path between the initial and final locations assuming that all system parameters are optimized except the trajectory  $\mathbf{Q}$ . The third trajectory considers that the UAV is hovering in a specific location for almost all the considered time  $T$ , except the time required to reach the desired location and the flying time to the final location. A simple interpretation of the ARIS trajectory is that the UAV tends to move closer to the BS and, where possible, to some users. This strategy likely aims to minimize average path-loss, which in turn minimizes the transmit power and, therefore, the exposure. In Table III, the corresponding exposure for the three considered trajectories is presented. We can see that the proposed trajectory achieves more than 70% and 30% reduction in EMF exposure compared to the direct trajectory and the one with the UAV hovering at a fixed location, respectively.

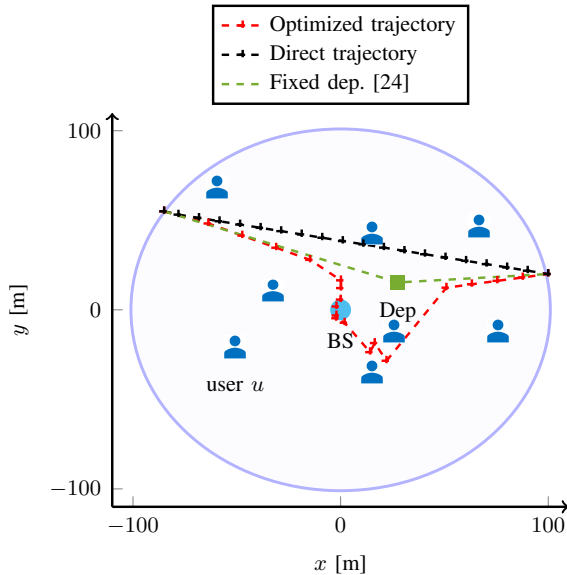


Fig. 3. Different trajectories of ARIS using different benchmark algorithms.

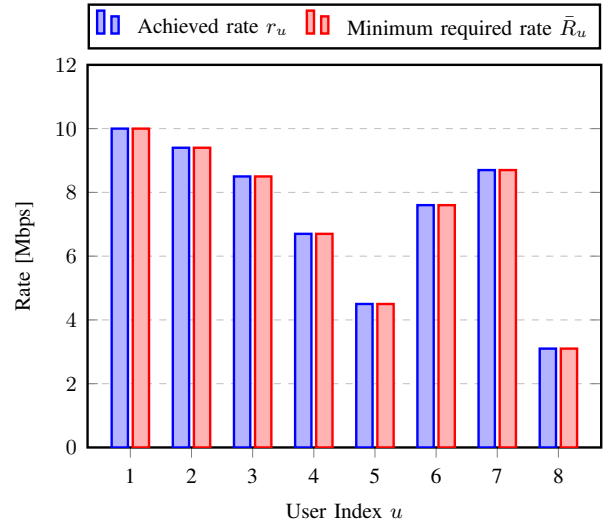


Fig. 4. Comparison of the achieved rate and the minimum required rate for the network users.

**TABLE III**  
AVERAGE UPLINK EXPOSURE ( $I$ ) VALUES FOR DIFFERENT ARIS TRAJECTORIES

Trajectory	Direct Path	Deployment	Optimized Path
$I$ [mW/Kg]	3.766	1.601	1.059
Reduction (%) w.r.t direct path	–	57.48	71.88

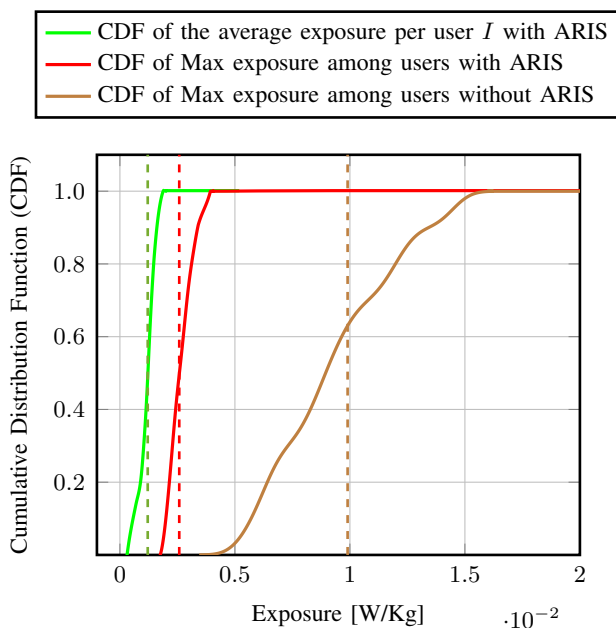


Fig. 5. The statistics of maximum and mean exposure among users.

This reduction is achieved while satisfying all rate constraints, as illustrated in Fig. 4. The proposed

solution effectively guarantees the fulfillment of QoS requirements while simultaneously minimizing the average uplink exposure.

It is worth noting that the introduction of ARIS to the network has a negligible effect on the exposure of neighboring users, as the ARIS trajectory is confined within the boundaries of the cell. Moreover, the proposed EMF-aware scheme effectively minimizes the mean exposure across users without increasing individual exposure levels. As shown in Fig. 5, the maximum exposure without ARIS is significantly higher than that with ARIS. For example, the probability that the maximum exposure with ARIS stays below 10 mW/Kg (which is the mean of the maximum exposure without ARIS) is almost 1. Additionally, even in the worst-case scenario, the maximum exposure under ARIS remains below 5 mW/Kg even when the probability is at its highest level, i.e., equal to 1.

#### B. Impact of the Number of BS Antennas and RIS Elements

In Fig. 6, we evaluate the impact of the number of antennas at the BS  $M_t$  on the average uplink expo-

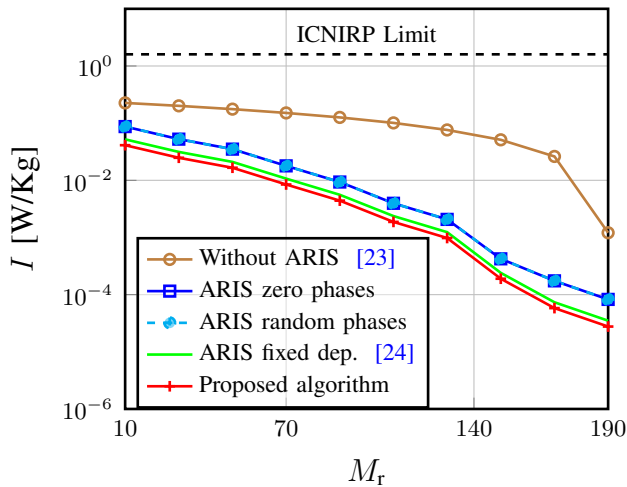


Fig. 6. Average uplink exposure  $I$  as a function of the number of receiving antennas  $M_r$  for various methods.

sure  $I$ . The results show that the exposure decreases logarithmically when the number of receiving antennas increases. Increasing the number of antennas at the BS improves receive diversity and enhances channel quality. This enables reducing the population's exposure while maintaining the required QoS. The proposed algorithm results reveals that using ARIS considerably reduces the exposure compared to the fixed RIS, which can provide at least 30% EMF exposure reduction for  $M_t = 32$ . Therefore, using ARIS can more effectively restrict exposure to meet specific requirements, making it particularly beneficial in environments where limited exposure is crucial, such as schools and hospitals [15]. This reduction is attributed to the inherent advantages of UAV mobility, which enhances the overall performance of the system. The high mobility allows the UAV to dynamically navigate along an optimal trajectory, thereby minimizing the population's exposure to the radio frequency (RF) radiations.

Fig. 7 characterizes the effect of different numbers of RIS reflecting elements on the Average uplink exposure of the network  $I$ . For this evaluation scenario, we assume that the minimum required data rate for all the network users is established at  $\bar{R}_u = 6$  Mbps,  $\forall u \in \mathcal{U}$ . Here, we observe that increasing  $N$  yields a better performance in terms of exposure reduction. However, for low values of  $N$ , the reduction is not significant. This can be attributed to the fact that low values of  $N$  do not effectively enhance the channel, and therefore do

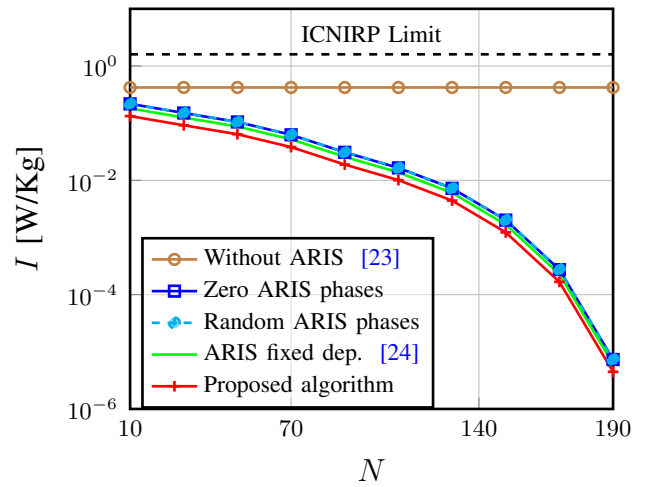


Fig. 7. Average uplink exposure  $I$  as a function of the number of RIS elements  $N$  for various methods.

not significantly reduce the transmit power allowing for lower exposure level. In contrast, for  $N \geq 100$ , the observed reduction is substantial, nearly an order of magnitude lower compared to the scheme where RIS is not used. This outcome highlights the effectiveness of RIS in mitigating uplink EMF exposure when a high number of RIS elements are employed.

## V. CONCLUSION

In this paper, we introduced a novel architecture incorporating ARIS to mitigate the potential risks associated with EMF exposure in uplink transmission of a MU-MIMO system. We proposed a two-fold design where we utilized the ARIS to establish non-direct LoS paths allowing lower transmit power, and to control the transmit beamforming allowing lower induced SAR reference. In our scheme, which incorporates ARIS mobility, the proposed solution ensures effective reduction of EMF exposure through the optimization of the transmit beamforming, RE allocation, RIS phase-shift vector, the transmit power, and the ARIS trajectory while maintaining the required data rate for users. The simulation results confirmed the performance of the proposed algorithm, demonstrating a significant reduction in the EMF exposure, i.e., for 6 Mb/s required UL compared to the scheme without RIS. These findings make our proposed architecture highly relevant to the general public, cellular operators, and the research community, as it offers a sustainable solution to mitigate the potential impacts associated with EMF exposure.

## APPENDIX A

## POWER OPTIMIZATION USING LAGRANGIAN METHOD

The Lagrangian of the convex optimization problem (37) is

$$\begin{aligned} \mathcal{L}(\mathbf{p}_u, \mu, \lambda) = & \sum_{n=1}^{N_c} \delta_{u,n} \left( \overline{\text{SAR}}_{u,n} p_{u,n} \right. \\ & \left. + \mu (\bar{R}_u - r_u(\mathbf{\Gamma})) + \lambda \left( \sum_{n=1}^{N_c} \delta_{u,n} p_{u,n} - P_{\max} \right) \right), \end{aligned} \quad (53)$$

where  $\mu$  and  $\lambda$  denote the Lagrangian multipliers associated with (37b) and (37c), respectively. Noting that the Lagrangian function is convex w.r.t  $\mathbf{p}_u$ , the optimal solution for this problem needs to satisfy the following KKT conditions

$$\begin{cases} \frac{\partial \mathcal{L}(\mathbf{p}_u, \mu, \lambda)}{\partial \mathbf{p}_u} = \mathbf{0}, \\ \mu (\bar{R}_u - r_u(\mathbf{\Gamma}_{u,n})) = 0, & \mu \geq 0, \\ \lambda \left( \sum_{n=1}^{N_c} \delta_{u,n} p_{u,n} - P_{\max} \right) = 0, & \lambda \geq 0. \end{cases} \quad (54)$$

Taking the derivative of  $\mathcal{L}$  w.r.t  $p_{u,n}$ , we obtain

$$\frac{\partial \mathcal{L}(\mathbf{p}_u, \mu, \lambda)}{\partial p_{u,n}} = \delta_{u,n} \left( \frac{w \overline{\text{SAR}}_{u,n} \mu \gamma(\mathbf{\Gamma}_{u,n})}{\ln(2)(\sigma^2 + p_{u,n} \gamma(\mathbf{\Gamma}_{u,n}))} + \lambda \right). \quad (55)$$

Then, based on (55), we can derive the optimal power as (38). On the other hand, the optimal  $\mu^*$  and  $\lambda^*$  can be numerically obtained by solving (54).

## APPENDIX B

## SCA FOR ARIS TRAJECTORY DESIGN

The first-order Taylor expansions of (50), (47), and (48) at given feasible points  $(\mathbf{u}_u^0, \mathbf{v}^0)$  can be respectively expressed as

$$\begin{aligned} x_{u,n}^2[\ell] & \left( \frac{a_{u,n}[\ell]}{u_u[\ell]^{\kappa_1} v[\ell]^{\kappa_2}} + \frac{b_{u,n}[\ell]}{u_u[\ell]^{\frac{\kappa_1}{2}} v[\ell]^{\frac{\kappa_2}{2}}} \right) \\ & \leq x_{u,n}^2[\ell] (A_{u,n}[\ell] + B_{u,n}[\ell]), \end{aligned} \quad (56)$$

$$d_{uR}^2[\ell] + (u_u^0[\ell])^2 - 2 u_u^0[\ell] u_u[\ell] \leq 0, \quad \forall u \in \mathcal{U}, \forall \ell \in \mathcal{N}_{\mathcal{T}}^{[13]} \quad (57)$$

$$d_{RB}^2[\ell] + (v^0[\ell])^2 - 2 v^0[\ell] v[\ell] \leq 0, \quad \forall \ell \in \mathcal{N}_{\mathcal{T}}, \quad (58)$$

where

$$\begin{aligned} A_{u,n}[\ell] = & a_{u,n}[\ell] \left( \frac{1}{(u_u^0[\ell]^{\kappa_1} + (v^0[\ell])^{\kappa_2})} \right. \\ & \left. + \frac{\kappa_1 (u_u[\ell] - u_u^0[\ell])}{(u_u^0[\ell]^{\kappa_1+1} + v[\ell]^{\kappa_2})} - \frac{\kappa_2 (v[\ell] - v^0[\ell])}{u_u[\ell]^{\kappa_1} + (v^0[\ell])^{\kappa_2+1}} \right), \end{aligned} \quad (59)$$

and

$$\begin{aligned} B_{u,n}[\ell] = & b_{u,n}[\ell] \left( \frac{1}{(u_u^0[\ell]^{\frac{\kappa_1}{2}} + (v^0[\ell])^{\frac{\kappa_2}{2}})} \right. \\ & \left. + \frac{-\frac{\kappa_1}{2} (u_u[\ell] - u_u^0[\ell])}{(u_u^0[\ell]^{\frac{\kappa_1}{2}+1} + v[\ell]^{\frac{\kappa_2}{2}})} - \frac{\frac{\kappa_2}{2} (v[\ell] - v^0[\ell])}{u_u[\ell]^{\frac{\kappa_1}{2}} + (v^0[\ell])^{\frac{\kappa_2}{2}+1}} \right). \end{aligned} \quad (60)$$

As such, (49) can be approximated as (51).

## REFERENCES

- [1] R. Nyberg *et al.*, "5G appeal: Scientists and doctors warn of potential serious health effects of 5G," 2017.
- [2] L. Chiaraviglio *et al.*, "Health Risks Associated With 5G exposure: A view from the communications engineering perspective," *IEEE Open Journal of the Communications Society*.
- [3] "France halts iPhone 12 sales over radiation levels," *BBC News*, Sep.13,2023. [Online]. Available: <https://www.bbc.com/uk/news/technology-66795168>
- [4] T. E. Aldrich *et al.*, "Electromagnetic fields and public health," *Environmental health perspectives*, vol. 75, pp. 159–171, 1987.
- [5] M. A. Jamshed *et al.*, "A Survey on Electromagnetic Risk Assessment and Evaluation Mechanism for Future Wireless Communication Systems," *IEEE Journal of Electromagnetics, RF and Microwaves in Medicine and Biology*, vol. 4, no. 1, pp. 24–36, 2020.
- [6] A. Elzanaty *et al.*, "5G and EMF exposure: Misinformation, open questions, and potential solutions," *Frontiers in Communications and Networks*, vol. 2, p. 635716, 2021.
- [7] P. Yinhui *et al.*, "Effect of cell phone radiation on neutrophil of mice," *International Journal of Radiation Biology*, vol. 95, no. 8, pp. 1178–1184, 2019.
- [8] N. T. Program *et al.*, "Toxicology and carcinogenesis studies in B6C3F1/N mice exposed to whole-body radio frequency radiation at a frequency (1,900 MHz) and modulations (GSM and CDMA) used by cell phones," *National Toxicology Program Technical Report Series*, no. 596, 2018.
- [9] A. Ahlbom *et al.*, "Possible effects of electromagnetic fields (EMF) on human health-opinion of the scientific committee on emerging and newly identified health risks (SCENIHR)," *Toxicology*, vol. 246, no. 2-3, pp. 248–50, 2008.
- [10] I. S. Group *et al.*, "Acoustic neuroma risk in relation to mobile telephone use: results of the INTERPHONE international case-control study," *Cancer epidemiology*, vol. 35, no. 5, pp. 453–464, 2011.
- [11] S. Larjavaara *et al.*, "Location of gliomas in relation to mobile telephone use: a case-case and case-specular analysis," *American journal of epidemiology*, vol. 174, no. 1, pp. 2–11, 2011.
- [12] IARC Working Group on the Evaluation of Carcinogenic Risks to Humans and others, "Non-ionizing radiation, Part 2: Radiofrequency electromagnetic fields," *IARC monographs on the evaluation of carcinogenic risks to humans*, vol. 102, no. PT 2, p. 1, 2013.
- [13] K. ITU-T recommendation, "Guidance on complying with limits for human exposure to electromagnetic fields," 2004.
- [14] I. C. on Non-Ionizing Radiation Protection *et al.*, "Guidelines for limiting exposure to electric fields induced by movement of the human body in a static magnetic field and by time-varying magnetic fields below 1 Hz," *Health physics*, vol. 106, no. 3, pp. 418–425, 2014.
- [15] L. Chen *et al.*, "Joint Uplink and Downlink EMF Exposure: Performance Analysis and Design Insights," *IEEE Transactions on Wireless Communications*, vol. 22, no. 10, pp. 6474–6488, 2023.
- [16] G. Castellanos *et al.*, "Multi-objective optimisation of human exposure for various 5G network topologies in Switzerland," *Computer Networks*, vol. 216, p. 109255, 2022.
- [17] L. Chiaraviglio *et al.*, "Dominance of smartphone exposure in 5g mobile networks," *IEEE Transactions on Mobile Computing*, vol. 23, no. 3, pp. 2284–2302, 2023.
- [18] Y. Qin *et al.*, "Unveiling passive and active EMF exposure in large-scale cellular networks," *IEEE Open Journal of the Communications Society*, vol. 5, pp. 2991–3006, 2024.
- [19] Q. Gontier *et al.*, "On the uplink and downlink emf exposure

- and coverage in dense cellular networks: A stochastic geometry approach,” *arXiv preprint arXiv:2312.08978*, 2023.
- [20] B. M. Hochwald *et al.*, “SAR codes,” in *2013 Information Theory and Applications Workshop (ITA)*. IEEE, 2013, pp. 1–9.
- [21] F. Héliot *et al.*, “Exposure modelling and minimization for multi-antenna communication systems,” in *2020 IEEE 91st Vehicular Technology Conference (VTC2020-Spring)*. IEEE, 2020, pp. 1–6.
- [22] M. Wang *et al.*, “Evaluation and Optimization of the Specific Absorption Rate for Multiantenna Systems,” *IEEE Transactions on Electromagnetic Compatibility*, vol. 53, no. 3, pp. 628–637, 2011.
- [23] F. Héliot *et al.*, “On the Exposure Dose Minimization of Multi-Antenna Multi-Carrier System Users,” *IEEE Transactions on Vehicular Technology*, vol. 71, no. 7, pp. 7625–7638, 2022.
- [24] H. Ibraiwish *et al.*, “EMF-Aware Cellular Networks in RIS-Assisted Environments,” *IEEE Communications Letters*, vol. 26, no. 1, pp. 123–127, 2022.
- [25] Z. Lin *et al.*, “Refracting RIS-Aided Hybrid Satellite-Terrestrial Relay Networks: Joint Beamforming Design and Optimization,” *IEEE Transactions on Aerospace and Electronic Systems*, vol. 58, no. 4, pp. 3717–3724, 2022.
- [26] —, “Pain Without Gain: Destructive Beamforming From a Malicious RIS Perspective in IoT Networks,” *IEEE Internet of Things Journal*, vol. 11, no. 5, pp. 7619–7629, 2024.
- [27] Y. Liu *et al.*, “Reconfigurable intelligent surfaces: Principles and opportunities,” *IEEE communications surveys & tutorials*, vol. 23, no. 3, pp. 1546–1577, 2021.
- [28] A. Kafizov *et al.*, “Wireless network coding with intelligent reflecting surfaces,” *IEEE Communications Letters*, vol. 25, no. 10, pp. 3427–3431, 2021.
- [29] Q. Wu *et al.*, “Intelligent reflecting surface-aided wireless communications: A tutorial,” *IEEE Transactions on Communications*, vol. 69, no. 5, pp. 3313–3351, 2021.
- [30] Y. Zeng *et al.*, “Wireless communications with unmanned aerial vehicles: opportunities and challenges,” *IEEE Communications Magazine*, vol. 54, no. 5, pp. 36–42, 2016.
- [31] L. Zhang *et al.*, “A Survey on 5G Millimeter Wave Communications for UAV-Assisted Wireless Networks,” *IEEE Access*, vol. 7, pp. 117460–117504, 2019.
- [32] Z. Lin *et al.*, “Supporting IoT With Rate-Splitting Multiple Access in Satellite and Aerial-Integrated Networks,” *IEEE Internet of Things Journal*, vol. 8, no. 14, pp. 11123–11134, 2021.
- [33] Z. Lou *et al.*, “Green tethered UAVs for EMF-aware cellular networks,” *IEEE Transactions on Green Communications and Networking*, vol. 5, no. 4, pp. 1697–1711, 2021.
- [34] W. Wang *et al.*, “Joint precoding optimization for secure SWIPT in UAV-aided NOMA networks,” *IEEE Transactions on Communications*, vol. 68, no. 8, pp. 5028–5040, 2020.
- [35] S. Li *et al.*, “Reconfigurable intelligent surface assisted UAV communication: Joint trajectory design and passive beamforming,” *IEEE Wireless Communications Letters*, vol. 9, no. 5, pp. 716–720, 2020.
- [36] K.-C. Chim *et al.*, “Investigating the impact of smart antennas on SAR,” *IEEE Transactions on Antennas and Propagation*, vol. 52, no. 5, pp. 1370–1374, 2004.
- [37] K. Shen *et al.*, “Fractional programming for communication systems—Part I: Power control and beamforming,” *IEEE Transactions on Signal Processing*, vol. 66, no. 10, pp. 2616–2630, 2018.
- [38] Z.-Q. Luo *et al.*, “Semidefinite relaxation of quadratic optimization problems,” *IEEE Signal Processing Magazine*, vol. 27, no. 3, pp. 20–34, 2010.
- [39] I. CVX Research, “CVX: Matlab Software for Disciplined Convex Programming, version 2.0,” <http://cvxr.com/cvx>, Aug. 2012.
- [40] J. Mirza *et al.*, “Channel Estimation Method and Phase Shift Design for Reconfigurable Intelligent Surface Assisted MIMO Networks,” *IEEE Transactions on Cognitive Communications and Networking*, vol. 7, no. 2, pp. 441–451, 2021.
- [41] J. He *et al.*, “Channel Estimation for RIS-Aided mmWave MIMO Systems via Atomic Norm Minimization,” *IEEE Transactions on Wireless Communications*, vol. 20, no. 9, pp. 5786–5797, 2021.
- [42] A. S. Alwakeel *et al.*, “Semi-Blind Channel Estimation for Intelligent Reflecting Surfaces in Massive MIMO Systems,” *IEEE Access*, vol. 10, pp. 127783–127797, 2022.
- [43] S. Boyd *et al.*, *Convex Optimization*. Cambridge, UK: Cambridge University Press, 2004.
- [44] Federal Aviation Administration, “Summary of Small Unmanned Aircraft Rule,” [https://www.faa.gov/uas/media/Part\\_107\\_Summary.pdf](https://www.faa.gov/uas/media/Part_107_Summary.pdf), 2017, accessed: May. 13, 2024.
- [45] S. Li *et al.*, “Reconfigurable Intelligent Surface Assisted UAV Communication: Joint Trajectory Design and Passive Beamforming,” *IEEE Wireless Communications Letters*, vol. 9, no. 5, pp. 716–720, 2020.
- [46] Technical Specification Group Radio Access Network, “Ts 38.455: NR positioning protocol a (NRPPa),” 3GPP, Tech. Rep. V16.1.0, Sep. 2020.
- [47] “Evolved universal terrestrial radio access (E-UTRA); further advancements for E-UTRA physical layer aspects (release 9),” Mar. 2010.
- [48] AWTG. (Accessed 2024) 5G Spectrum UK. Online; accessed April 2024. [Online]. Available: <https://www.awtg.co.uk/5g-spectrum-uk>